EUROPEAN FUSION DEVELOPMENT AGREEMENT

EFDA–JET–PR(01)20

M Mattioli et al

Experimental and Simulated VUV Spectra from the JET Tokamak and the Reversed Field Pinch RFX

Experimental and Simulated VUV Spectra from the JET Tokamak and the Reversed Field Pinch RFX

M Mattioli[1], K B Fournier[2], M E Puiatti[1], M Valisa[1], L Carraro[1], I Coffey[3], M O'Mullane[4], F Sattin[1], P Scarin[1].

EURATOM/UKAEA Fusion Association, Culham Science Centre,
Abingdon, Oxfordshire, OX14 3DB, UK.
[1]Associazione Euratom-ENEA sulla Fusione, Consorzio RFX, Padova, Italy.
[2]Lawrence Livermore National Laboratory, P O Box 808, L-41 Livermore, CA94550, USA.
[3]Queens University, Belfast BT7 1NN, Northern Ireland.
[4]University of Strathclyde, Glasgow, G4 0NG, UK.

EXPERIMENTAL AND SIMULATED VUV SPECTRA FROM THE JET TOKAMAK AND THE REVERSED FIELD PINCH RFX.

M.Mattioli[1], K.B. Fournier[2], M.E. Puiatti[1], M.Valisa[1], L. Carraro[1], I. Coffey[3], M. O'Mullane[4], F. Sattin[1], P. Scarin[1]

[1]*Associazione Euratom-ENEA sulla Fusione, Consorzio RFX, Padova, Italy*
[2] *Lawrence Livermore National Laboratory, PO Box 808, L-41 Livermore, Ca 94550, USA*
[3]*Queens University, Belfast BT7 INN, North Ireland*
[4]*University of Strathclyde, Glasgow G4 0NG, UK*

Abstract

Experimental VUV spectra from the JET tokamak and from the reversed field pinch RFX have been simulated. For the former device both n=2 to n=2 L-shell Ar and Ne spectra (respectively, in the 14.5-43.0 and in the 35.0-80.0 nm ranges) were considered, whereas for RFX only the Ne spectrum was available. The spectra have been observed with the SPRED spectrometer. From the simulation of the spectra, relative sensitivity curves have been obtained for each instrument in the ranges of the simulation. For RFX only, it has been possible to extend this curve from ~13.0 to ~105 nm, by simulating intrinsic C and O emissions. The photon emission coefficients of the lines with wavelengths in the ranges of the experimental spectra were obtained from collisional-radiative models. For Ar and Ne these coefficients have been calculated by the HULLAC atomic physics codes, whereas for C and O the corresponding coefficients have been taken from the ADAS database. Impurity modelling is performed using a one-dimensional impurity transport code, calculating for each atomic species the radial distribution of the impurity ions. The line brightnesses are evaluated in a post-processing subroutine

and the simulations of the spectra are obtained. The spectral simulations (including impurity ion transport) give confidence in the atomic physics calculations, and allow the determination of the transport coefficients in the plasma regions from which the considered ionisation states emit. Finally, the obtained relative sensitivity curves of the two SPRED spectrometers have been compared with the calibrations performed by means of the branching ratio technique.

1. Introduction

Intrinsic and/or purposely seeded impurities are always present in magnetic confinement fusion (MCF) devices. Experimental impurity X-ray and XUV spectra have been observed for a long time, but, until quite recently simulations of a full spectrum were very scarce, with the exception of K-shell spectra (i. e., the satellite spectra associated with the He-like resonance lines) [1-3]. As discussed in Ref. [4], the analysis of spectra emitted by hot and well diagnosed MFC plasmas is important since it touches atomic physics issues that are required for simulation codes to be used in the analysis of high spectral resolution data from X-ray telescopes. Neglecting new line identification, most of the work in MCF devices is usually dedicated to the determination of the plasma chemical composition (i. e., the identification of the impurity elements and the evaluation of their concentration) and to the evaluation of the impurity transport parameters, namely the diffusion coefficient and the convection velocity. For this purpose only a few selected strong lines are considered and are simulated using impurity ion transport codes (see, e. g., Ref. [5]).

Analyses, including full spectral simulation of n=2 to n=3 L-shell neon and argon emission spectra have been reported in Refs [6-7]. Neon emission in

the 10 nm region has been observed both in the TS tokamak and in the reversed field pinch RFX, whereas argon emission in the 2.3-3.4 nm region has been observed in the JET tokamak. The analysed Ne spectra include lines from three ionisation states, Ne^{7+}, Ne^{6+}, and Ne^{5+}, ions belonging to the Li-like, Be-like and B-like isoelectronic sequences, whereas the analysed Ar spectrum includes lines from five ionisation states from Li-like Ar^{15+} to N-like Ar^{11+}. In both cases impurity modelling has been performed using a one-dimensional (1D) impurity transport code that calculates the steady state radial distribution of the Ne or Ar ions. The line brightnesses have been evaluated in a post-processing subroutine which simulates the spectra. For the latter purpose collisional radiative (CR) models have been built for the ions whose lines are observed in the spectra, considering electron collisional excitation and radiative decay as the populating processes of the excited states. These models give photon emission coefficients (PECs) for the emitted lines at electron density and temperature values corresponding to the experimental situations. While the parts of the spectra corresponding to a single ionisation state do not depend on the experimental conditions, the superposition of these partial spectra is connected to the ion charge distribution, which depends on the radial profiles of the electron density and temperature and on the impurity transport coefficients.

In this paper the n=2 to n=2 L-shell spectra from Ne and Ar are reported, the former from both the JET tokamak and the reversed field pinch RFX, whereas the latter only from the JET tokamak. Both spectra have been observed by a VUV survey spectrometer (SPRED) [8], whose relative and absolute sensitivity calibrations as a function of the wavelength were rougly measured by the branching ratio technique. The simulation of the spectra has allowed the evaluation of relative sensitivity curves from ~15 up to ~80 nm for the JET instrument. For the RFX instrument it has been possible to extend this

curve from ~13.0 nm up to ~105 nm by simulating intrinsic C and O. It has not been possible to do the same for the JET tokamak since in this elliptical device (most of the time operated with a divertor) the low ionisation C and O ion emission comes essentially from the divertor region, and is therefore poloidally localized. The calculated sensitivity curves , compared with the experimental branching ratio calibrations, have shown a good agreement.

The paper is organised as follows: the experimental conditions in both devices are presented in section 2 along with the spectra to be simulated. The CR models and the impurity modelling have already been discussed elsewhere [6, 7] and they will be only briefly recalled, respectively, in sections 3 and 4. In sections 5 and 6 the experimental and simulated spectra are compared, respectively, for JET and RFX. The relative sensitivity calibration curves for the two SPRED spectrometers are presented in section 7, which is totally addressed to the calibration techniques; the curves found are compared with other experimental findings for SPRED spectrometers. A summary is given in section 8 with conclusive remarks concerning both the atomic physics involved in the simulated spectra and the difficulties of reliable sensitivity calibrations of the VUV spectrometers.

2. Experimental data

2.1 Neon and argon spectra from the JET tokamak

The plasma of the JET tokamak is characterised by an approximately elliptical cross section (minor radius a_L=0.95 m, plasma half height b_L=1.75 m, major radius R_0=2.85 m, plasma elongation b_L/a_L =1.85), a maximum plasma current I_p=6 MA and a toroidal magnetic

field (at R_0) B_t=3.8 T. Neutral beam injection (NBI), ion cyclotron resonance heating (ICRH) and lower hybrid current drive (LHCD) are available for supplementary heating. Limiter as well as divertor discharges are possible; the present version of the single null (bottom X-point) divertor is MkIIGB. Intrinsic impurity spectra before seeding indicate that the discharge pollution is dominated by carbon ions.

The electron density profiles $n_e(r)$ are obtained from the Lidar Thomson backscattering diagnostic, with the addition of peripheral data from a laser interferometry beam crossing the plasma on the inner side of the last closed magnetic surface (LCMS). In the plasma interior the electron temperature profiles $T_e(r)$ are measured by the Lidar Thomson backscattering diagnostic and by an electron cyclotron emission (ECE) heterodyne. On the other hand, near the LCMS, and a few centimetres inside, the T_e the values from the edge Lidar Thomson backscattering system are preferred.

Two experimental, horizontal line of sight spectra are shown in Fig. 1. They have been detected by the SPRED spectrometer [8], respectively, in Ar (top) and Ne (bottom) seeded single null diverted L-mode discharges characterised by the following parameters: I_p=2.4 MA, B_t=3.0 T, D_2 filling gas, Deuterium NBI power P_{NBI} ~5 MW. The n_e and T_e profiles are similar for the two discharges, with central values $n_e(0)$ 3.0 10^{19} m^{-3} and $T_e(0)$ 5.6 keV for the Ne seeded discharge and $n_e(0)$ 2.6 10^{19} m^{-3} and $T_e(0)$ 5 keV for the Ar seeded discharge. Both spectra are the average of several acquisitions obtained with a read-out time of 35 ms during a one-second interval around the time of maximum emission in the seeding gas line brightnesses. For the various spectral features the Roman numerals indicate the spectroscopic notations of the dominant Ar or Ne ions.

Shorter wavelength spectra are obtained simultaneously with the Schwob-Fraenkel extreme grazing incidence vacuum spectrometer, which also views the plasma along a central line of sight [9]. The Ar spectrum between 2.3 and 3.4 nm has already been simulated and presented in Ref [7], whereas the Ne spectrum between ~9.5 and ~13.0 nm is similar to the spectra obtained with the SPRED spectrometer in other MCF devices and presented in Ref [6]. The Ar spectrum between 2.3 and 3.4 nm includes lines from five ionisation states, namely from Li-like Ar^{15+} to N-like Ar^{11+}, whereas the Ne spectrum in the range 9.5-13 nm includes lines from three ionisation states, namely from Li-like Ne^{7+} to B-like Ne^{5+} ions.

2.2 Neon and intrinsic carbon plus oxygen spectra from the reversed field pinch RFX

RFX is a large reversed field pinch (minor radius a_L=0.46 m, major radius R=2.0 m) designed to operate with a plasma current I_p up to 2 MA (currently operated with I_p=0.5-1 MA). The central toroidal magnetic field is 0.5-1 T. No additional heating system is installed, as is common to RFP devices. The inconel vacuum vessel is almost completely covered with carbon tiles; carbon and oxygen are, therefore, the main impurities, metalic impurities being reduced to very low levels. The $n_e(r)$ and $T_e(r)$ profiles are obtained, respectively, by a multichord CO_2 laser interferometer and by a Thomson scattering system complemented by a Si-Li X-ray detector and a double-filter soft X-ray monitor [10].

Two experimental, horizontal line of sight spectra are shown in Fig. 2. They have been detected by the SPRED spectrometer (as on JET) in a Ne seeded hydrogen discharge (top) with $n_e(0) = 3.7\ 10^{19}\ m^{-3}$ and $T_e(0)$ = 210 eV and in a non-seeded discharge (bottom) with $n_e(0) = 5.\ 10^{19}\ m^{-3}$ and $T_e(0)$ =

190 eV. In the latter spectrum, only intrinsic impurity (i., e., C and O) lines are detected. The Ne spectrum between 6.0 and 13.5 nm, obtained in a similar discharge with the Schwob-Fraenkel spectrometer, has been presented and simulated in Ref. [6].

3. Atomic struture calculations and collisional-radiative models

For Ne and Ar the (steady-state) CR photon emission coefficients (PECs) have been computed as already discussed in Refs [6] and [7]. Each ion has been treated independently from the others ignoring ionisation and recombination into and out of the ground and excited energy levels. The steady state level populations are found by inverting the full CR rate matrix for each ion [11]. The atomic data used in constructing the emission models for each ion are generated from *ab initio* calculations with the Hebrew University Lawrence Livermore Atomic Codes (HULLAC), which evaluate both electron excitation rate coefficients (integrating the distorted wave approximation cross sections over a Maxwellian distribution of free electron energies) and radiative transition probabilities. Both are entered into the CR model, which evaluates the relative populations for the levels of each ion at steady state by solving the well-known coupled set of rate equations.

The final outcome of the code is the photon emission coefficient (PEC) in units of photons m^3 s^{-1} for a given transition j -> i with transition probability $A_{j,i}$

$$P_{j,i} = \frac{n_j}{n_e} \sum A_{j,i} \quad , \qquad (1)$$

where nj is the normalised (for each ion) relative population of level j and the sum over the A rates is over all multipoles connecting the two levels in question, with the electron density n_e divided out of the model. The PECs have

been evaluated for a n_e range corresponding to the densities found in the MCF devices, whereas for T_e the ranges are related to the electron temperatures of the emitting layers of the considered ions. The wavelengths λ of the lines have been taken in the Kelly' s book [12]. For Ar the values given in the NIST databank [13] have been used when some λs were missing in Ref.[12]. To simulate the spectra in Figs 1 and 2, it has been necessary to evaluate the PECs for more ionisation states than those already considered for the spectra of Refs [6] and [7]. In fact, the Ne spectra include lines from six ionisation states, namely from Li-like Ne^{7+} to O-like Ne^{2+} ions, whereas the Ar spectra include lines from seven ionisation states, namely from Li-like Ar^{15+} to F-like Ar^{9+} ions.

Specific calculations were not necessary for the simulations of the C and O spectra, since the relevant PECs were found within the atomic physics database "Atomic Physics and Analysis Structure" (ADAS) [14,15]. Two kinds of PECs are available there: with metastables resolved or unresolved. In the former case the metastable states are considered as independent highly populated levels, whereas in the second model there is only a single ground state. We have taken the unresolved PECs obtained with the projected matrix method.

4. Impurity modelling

The impurity transport simulation code describes in cylindrical geometry ionisation, recombination and radial transport of the ions of a given atomic species. The following system has to be solved:

$$\partial n_z/\partial t = -(1/r)\,[\partial\,(r\Gamma_z)/\partial r] + n_e\,(n_{z-1}S_{z-1} - n_z S_z + n_{z+1}\,\alpha_{z+1} - n_z\,\alpha_z) \qquad z=0,\,1,\ldots.,\,Z_N \qquad (2)$$

where Γ_z is the radial particle flux density (positive when directed outwards) of the ions of charge z for the atomic species with nuclear charge Z_N, and n_z is the corresponding ion density. S_z and α_z are, respectively, for the ions of charge z the ionisation rate coefficients and the radiative plus dielectronic recombination rate coefficients. The ionisation and recombination rates used in system (2) have been discussed for Ar, Ne and O plus C, respectively, in Refs [7, 6 and 16]. Since the JET plasma is non circular, the so-called Vprime function $V_p'(r)=dV_p(r)/dr$ is introduced in the radial diffusion term instead of r, where $V_p(r)$ is the volume inside the magnetic surface of radius r. Then the first term in the rhs of system (2) becomes $(1/V_p') [\partial(V_p'\Gamma_z)/\partial r]$.

The impurity flux density Γ_z is expressed as the sum of both diffusive and inward convective terms

$$\Gamma_z(r) = - D(r) \partial n_z(r)/ \partial r - V(r) n_z(r) \qquad (3)$$

where D(r) and V(r) are the radially dependent diffusion coefficient and inward convection velocity, respectively, both taken independently of the charge of the ions. For the special case of a radially constant D, taking $V(r)=(r/a) V_A$ (a being the last mesh radius) yields at steady state a Gaussian profile for the total impurity density $n_t(r) = n_t(0) \exp(-S r^2/a^2)$, with a peaking parameter $S= a V_A/2 D$.

Previous RFX simulations [10,16] indicated that the charge-exchange (CX) recombination with neutral hydrogen isotopes must be included as a supplementary recombination process in system (2) to obtain agreement between experimental and simulated line ratios of C and O ions of the H-like and He-like isoelectronic sequences. Assessed CX cross sections and

recombination rates are available for C and O [17,18]. On the contrary, for Ne and Ar, data are available only for a few ionisation states, and, generally, the low energy cross section data available are insufficient to deduce reliable rates. Only scaled cross sections versus scaled energy have been proposed for ions of medium- and high-Z elements [18-20]. According to Janev et al. [18] the proposed formulae represent, with a r.m.s. deviation of 20%, all the available experimental cross section data in charge states $q \geq 5$ colliding with ground state neutral hydrogen isotopes. The scaling relations apply also for ions in charge states q=3 and 4 except for reduced energies $E/q^{1/2}$ below 100 eV/amu. We have compared for both Ne and Ar the cross sections predicted by the scaling formulae with experimental data found in Refs [21-23]. The conclusion is that, starting from q=3, in the range of energies of the order of 100 eV/amu the scaled cross section overestimate by a factor of 2-3 the available data for low charge ions (up to q=7 for Ne and q=10 for Ar [22]). For q=2 the overestimation, for both Ar and Ne, is larger by more than one order of magnitude. On the other hand, for higher energies the scaling formulae are a better representation of the CX recombination cross sections. The scaling relation given in Ref. [19], practically coincident with that of Ref.[18] has been used. As a consequence of all these uncertainties, we have, for the JET spectra, at first neglected CX recombination, as already done in Ref. [7] for Ar. The CX process has been added subsequently to determine if the physical conclusions change. On the other hand, for the RFX spectra, as already said, the inclusion of CX recombination has been necessary for the simulation of C and O line ratios with a neutral hydrogen density profile derived from experimental findings [10]. In section 6, the discussed uncertainties on the Ne data for CX recombination in the 100 eV/amu energy range will be considered by analysing, for neon, the effect of a reduction of the neutral density.

The analysed spectra have been obtained for constant line brightness conditions. Therefore it is possible to consider only a steady state solution of system (2); a recycling and pumping model is not necessary to achieve a realistic description of the peripheral source function. For JET, the presence of the divertor and the fact that Ne and Ar ions penetrate quite ionised to the interior of the LCMS is taken into account by a "thick" scrape-off layer SOL (δ_{SOL}= 0.05 m). The plasma radius for the simulations is then 1 m, i. e., half the horizontal dimension $2a_L$ of the LCMS plus δ_{SOL}.

5. Simulations of the n=2 to n=2 Ar and Ne spectra in JET

The Ar spectrum of figure 1 (top) has been obtained in the same discharge as the n=3-2 Ar spectrum in the 2.3-3.4 nm spectral range simulated in Ref. [7] and it includes lines from seven ionisation states from the Ar^{15+} Li-like to Ar^{9+} F-like ions, i. e., except the last two, the same as for the n=3-2 Ar spectrum. The simulation reported in Ref. [7] has been repeated with the addition of another post-process subroutine producing the n=2-2 simulated Ar spectrum. The choice of the transport coefficients D(r) and V(r) has been extensively reported in Ref. [7] and will be only briefly recalled here. The simulation is for steady state plasma conditions, then, at a first approximation, it is sensitive to the ratio of the two transport coefficients, i. e., to the previously defined peaking factor S. Moreover the Ar spectra are obviously sensitive to the distribution of the ion charge states in the plasma region where the emitting layers exist. Therefore, for instance, a central depression of both D(r) and V(r) cannot be proved with the available experimental data whereas to reproduce the emission spectra it has been necessary to introduce a peripheral

transport barrier by shaping either both D(r) and V(r) or just one of them on the inner side of the LCFS. The results presented in Ref. [7] were obtained with a predominantly diffusive barrier (obtained by reducing D(r)), but the possibility of good simulations by means of a convective barrier (obtained by increasing V(r)) was reported as well. The successive radial shaping of V(r) is such that the peaking factor S becomes 0 in the plasma core with a resulting flat total Ar density profile. With these transport parameters the Ar XI and Ar X peak emissivities are localised around the LCMS at r=0.95 m, whereas the more ionised ions have all their peak emissivities inside the LCMS. More details on these spectra simulations, e. g. the effect of varying the core D values, can be found in Ref. [7].

Figure 3 shows normalised experimental and simulated spectra (full and broken curves, respectively) for a Gaussian instrumental function having a full width half maximum (FWHM) equal to 0.45 nm. The spectrometer resolution being relatively low, the Ar charge states contributing to the spectrum of figure 3 need to be clarified. Figure 4 shows seven normalised simulated spectra (with FWHM of 0.03 nm) each emitted by a single ionisation state from Ar^{15+} to Ar^{9+} (from top to bottom). Note that for Ar^{14+}, with a strong singlet line at 22.115 nm, the ordinate scale has been expanded to show the other weaker lines. As subsequently shown, the spectrometer sensitivity is practically constant in the wavelength range of the Ar spectrum of figure 3. Similarly to figures 3 and 4, figure 5 shows the normalised experimental and simulated spectra and figure 6 shows six normalised spectra from calculations, each emitted by a single ionisation state from Ne^{7+} to Ne^{2+} (from top to bottom).

For the final Ne simulation, figure 7 shows the radial profiles of a) n_e and T_e; b) D and V; c) a few Ne ion densities (Ne^{4+} to Ne^{10+}) n_z, normalised to the total Ne ion density; and d) the emissivities (normalised) E_{nor} of a few Ne

V to Ne VIII lines. In distinction to the Ar spectrum of figure 3, the Ne peak emissivities of all the ionisation states contributing to the spectrum in figure 5 are located outside the LCMS at r=0.95 m. Compared to the Ar seeded discharge the convective barrier has been slightly "weakened" by increasing D from 0.13 to 0.18 m^2/s outside the LCFS. In this way a good simulation of the 10 nm Ne spectrum has been obtained (see later). To simulate the spectrum of figure 5, the SPRED spectral sensitivity (discussed in section 7) as a function of the wavelength λ has been varied to obtain the best agreement between experiment and calculation.

In figure 8, the experimental and simulated Ne spectra, top and bottom, respectively, between 9.6 and 12.9 nm are shown. As already mentioned, the peripheral diffusion barrier has been finely adjusted to obtain good relative amplitudes of the three strongest lines of Ne VIII, VII and VI at 9.8, 10.6 and 12.26 nm, respectively. However, as far as the other weaker lines are concerned, the global simulation of the Ne spectrum is not as good as for the spectra reported in Ref. [6]. The discrepancies are mainly due to the uncertainty on the values of n_e and T_e in the emitting layers of the considered Ne ions, which are located just outside the LCFS. The fact that the simulated Ne VIII 10.3 nm line is too weak indicates that the assumed T_e values in the emitting shell could be too high. Similarly, the fact that the simulated amplitudes of three strongest singlet Ne VII lines, at 9.7, 11.6 and 12.7 nm, are too large indicates that the assumed n_e values in the emitting shell could be too low. Both statements are justified by the dependence of the Ne VIII and Ne VII PECs on T_e and n_e, respectively (as shown in figure 3 and in figure 4 of Ref. [6]). Consequently, the SOL plasma is probably more dense and less warm than assumed. Unfortunately, for the considered JET discharges no n_e and T_e experimental data (e. g., with reciprocating Langmuir probes) were available.

The n_e value around the LCMS is about 10^{19} m^{-3}, this value should be probably multiplied by 1.5-2 to approach the n_e values in the Ne VIII-VII emitting shells for the experimental conditions reported in Ref. [6]. At the same time, increasing n_e, the emitting shells are displaced towards lower T_e values, possibly avoiding a simultaneous reduction of T_e (r).

Quantitatively, proceeding as in Ref. [7], the central Ne density has been estimated to be about 1.0 10^{18} m^{-3}, whereas the central carbon density is always of the order of 2.2 10^{17} m^{-3}.

Including the CX recombination in equation (2), no significant differences have been observed in the simulated Ar spectrum in the 14.5-43.0 nm range. This is checked by assuming a deuterium density of a few 10^{15} m^{-3} in the SOL (i. e., of the same order as found on the equatorial plane in DIII-D L-mode divertor discharges [24]). This is consistent with what was observed in Ref. [7] for the n=3-2 Ar spectrum in the 2.3-3.4 nm range. Using the same neutral profile, the same conclusion is not valid for the two previously simulated Ne spectra. The observed differences were too large, unless the deuterium density is reduced to the order of 10^{15} m^{-3} in the SOL and at the same time the peripheral barrier is weakened by further increasing D from 0.18 to 0.22 m^2/s outside the LCFS. To conclude, given the uncertainties related to the CX cross sections discussed at the end of section 4 and since a measured value of the deuterium density is not available, we can only state that the physical conclusions reached concerning the seeding impurity transport in the Jet edge plasma cannot be modified by the CX recombination.

6. Simulations of the SPRED spectra in RFX

Recent RFX impurity studies have indicated that D(r) is flat for most of the radius and is decreasing near the plasma border, producing a peripheral diffusion barrier. The diffusion coefficient D is much larger than in tokamaks, in the range of 10 to 30 m^2/s. Since the n_e profile is either very flat or shallow with a peripheral peak, best agreement with the spectroscopic data is obtained with a convection velocity V outward on most of inner radius, becoming inward at the periphery with a maximum value from 20 to 80 m/s [10]. The two RFX spectra shown in figure 2 have been simulated using such radial dependencies of D(r) and of V(r) and with a Gaussian FWHM= 0.4 nm. The bottom spectrum is from one of the discharges considered in Ref. [10], then the same transport coefficient profiles have been assumed as given in the figure 7 of that reference. The n_e, T_e, D and V radial profiles are not presented, since they are similar to the corresponding profiles of the Ne seeded discharge to be discussed later. Considered intrinsic elements were C and O with central densities, respectively, of the order of 5.6 10^{17} m^{-3} and 2.6 10^{17} m^{-3}. The best-simulated spectrum, obtained by adjusting the spectrometer sensitivity between 12 and 105 nm, is shown in figure 9. All the missing lines (e. g., around 34 and 77 nm) are second order of C or O lines, the He II resonance line at 30.3 nm also being present. The shortest wavelength line included in the analysis is the O VI 12.8 nm line. The C VI Balmer α and β lines are also included, as well as the three n=2-3 C V triplet lines, with PECs from Ref. [16].

On the other hand, for the Ne seeded discharge a 10 nm spectrum being available, we proceeded as in the previous section: the peripheral transport barrier is finely adjusted to obtain good relative amplitudes of the three

strongest lines of Ne VIII, VII and VI with λ equal, respectively, to 9.8, 10.6 and 12.26 nm. Then the Ne spectrum of figure 2 top is simulated by adjusting the spectrometer sensitivity between 34 and 80 nm. The difference between the two sensitivity curves is negligible and a single curve will be presented in the section 7.

In figure 10, for the Ne seeded discharge the same parameters as in figure 7 for JET are plotted. In subset c the full curve is the He-like Ne^{8+} ion density (the Ne^{9+} and Ne^{10+} ion densities being negligible given the low electron temperature of RFX) and the Ne^{4+} to Ne^{7+} ion densities have been multiplied by 4. In figure 11 the SPRED spectrum of figure 2 top is compared with the simulation. The only large second order line is the He II resonance line at 2*30.3 nm. Finally, for the RFX 10 nm Ne spectrum figure 12 is the same as figure 8 for the corresponding JET spectrum. It has to be stressed that the "anomalies" of the JET spectrum, discussed in the previous section are not so prominent. The quality of the simulation is quite near to that of the simulations reported in Ref. [6]. This is a confirmation that the JET spectrum "anomalies" have to be associated with the lack of good peripheral n_e and T_e diagnostics, and not to the validity of the atomic physics data used. The simulation code gives the following central densities, respectively, for C, O and Ne: $1.0\ 10^{18}$, $6.6\ 10^{17}$ and $8.4\ 10^{17}\ m^{-3}$.

Concerning CXR for Ne, we proceeded as was done for the JET simulation. The neutral H density profile (maximum value at the last mesh ~$1.5\ 10^{17}\ m^{-3}$) has been divided by two to check the influence of the uncertainties of the Ne CX recombination cross sections. The variations of the simulated spectra were negligible and, for the same central Ne density, the Ne brightnesses were reduced by 10-15%.

7. Sensitivity of the SPRED spectrometers

The absolute sensitivity of the VUV spectrometers can be obtained by the branching ratio technique [8, 25-27] or by radiometric calibration on a synchrotron facility [25, 28]. The former method, which can be done in situ (thus permitting frequent checks of the calibration) and generally uses a second visible spectrometer observing the plasma along the same line of sight, is based on the measurement of the brightnesses of two spectral lines that originate from the same upper level and have a reliable known branching ratio. In this way relative sensitivities can be obtained, but, if the sensitivity at one wavelength is absolutely known, these measurements allow the absolute calibration of the instrument at the other wavelength. Branching ratio tables using lines from light elements can be found in Ref. [29]. However, to compensate for the lack of suitable sufficiently strong lines or because of accidental blendings in some intervals of the VUV range, it has been suggested to use either branching ratios of Cr to Mo magnetic dipole lines [26] or to use the relative intensities of lines produced in the radiative cascades of excited levels populated by CX recombination of fully stripped C to O ions with high energy neutral beams [30, 31]. Effective emission cross sections, including the contribution of cascades, are computed from theoretical CX cross sections and from the highly accurate transition probabilities for hydrogenic ions. The visible spectrometer is usually absolutely calibrated against blackbody (e. g., using a W ribbon lamp) or against D_2 lamps, absolutely calibrated in specialised facilities, as that used in Ref. [32] covering the range $\lambda \geq 120$ nm.

The relative inverse sensitivity curves obtained with the simulations described in the previous sections are shown in figure 13. They have been normalised at 30 nm and were calculated in photons/(s sr m^2) /(counts/s). The open circles are for the JET spectrometer and the full squares for the RFX

spectrometer. The inverse sensitivity data from branching ratio for the JET SPRED are also reported in fig.13 (dashed line); only two points (full squares) have been measured for RFX. All these data show quite a good agreement with the curves obtained from the simulations. The main difference between the two spectrometers lies below 30 nm, where the inverse sensitivity of the JET instrument is nearly constant, while for RFX decreases significantly. The curve calculated for RFX is more similar to that reported in [27] for the EXTRAP-T1 SPRED spectrometer. In fact in that case the inverse sensitivity decreases down to 15 nm, and increases again in the range 15-10 nm. In this last part of the SPRED spectrum the RFX curve could be affected by large errors: even if the simulation is still rather good, the spectrometer could be significantly affected by stray light near the zero order.

8. Conclusion

Experimental spectra obtained with the SPRED spectrometer on JET and RFX have been reported and simulated. They include both n=2 to n=2 L-shell Ne and Ar emissions: the former are observed in both the JET tokamak and the reversed field pinch RFX, whereas the latter is only from the JET tokamak. The Ne and Ar spectra span, respectively, from 35 nm to 80 nm and from 15 nm to 43 nm. The analysed Ne spectra included lines from six neon ionisation states from Li-like Ne^{7+} to O-like Ne^{2+}, whereas the analysed Ar spectrum includes lines from seven Ar ionisation states from the Ar^{15+} Li-like to Ar^{9+} F-like ions. For RFX, intrinsic C and O spectra from 13 up to 105 nm have also been simulated.

The photon emission coefficients for the lines with wavelengths in the ranges of the experimental spectra were obtained from collisional-radiative

models (the HULLAC atomic physics code for Ar and Ne, the ADAS database for C and O). Impurity modelling is performed using a one-dimensional impurity transport code, calculating for each atomic species the radial distribution of the ions. The line brightnesses are evaluated in a post-processing subroutine and simulated spectra are obtained. The spectra simulations (including impurity ion transport) give confidence in the atomic physics calculations, moreover, they allow the determination of the transport coefficients in the plasma regions emitting the considered ionisation states. For both Ne and Ar the transport parameters (namely a diffusion coefficient and a convection velocity) are obtained by a companion simulation of the shorter wavelength n=2 to n=3 spectra of the same elements as done in previously reported analysis [6, 7]. Subsequently, the SPRED relative spectrometer sensitivity as a function of the wavelength has been adjusted to get the best agreement between simulated and experimental spectra. For RFX C and O spectrum the transport parameters have been taken as having been obtained in similar discharges and previously reported in Ref. [10]. The relative sensitivity curves have been obtained from ~15 up to ~80 nm for the JET instrument and from ~13.0 nm up to ~105 nm for the RFX instrument. Finally in section 7, the relative sensitivity curves of the two SPRED spectrometers have been compared with the calibrations performed on both instruments by means of the branching ratio technique. In the same section the difficulties of calibrating VUV instrument are discussed.

Acknowledgements

Part of this work has been done at JET (Culham, UK) under the European Fusion Development Agreement. Another portion of this work was performed under the auspices of the U.S. Department of Energy by Universityof California Lawrence Livermore National Laboratory under contract No. W-7405-Eng-48.

References

[1] Bitter M., Hsuan H., Hill K. W. and Zarnstorff M., 1993 Phys. Scr. T47 87

[2] Bombarda F., Giannella R., Källne E. et al 1988 Phys. Rev. A 37504

[3] Phillips K. J. H., Keenan F. P., Harra L. K. et al 1994 J. Phys B: At. Mol. Opt. Phys. 27 1939

[4] Fournier K. B., Finkenthal M., Pacella D. et al (2000) Proc. of the Workshop on Atomic Data Needs for X-ray Astronomy, NASA Publications (Bautista M., Kallman T. and Pradhan A. editors) 1127 (also:http://heasarc.gsfc.nasa.gov/docs/heasarc/atomic/)

[5] De Michelis C. and Mattioli M., 1984 Rep. Prog Phys. 47 1233

[6] Mattioli M., Fournier K., Carraro L. et al 2000 Phys. Rev. E 604760

[7] Mattioli M., Fournier K., Carraro L. et al 2001 J. Phys B: At. Mol.Opt. Phys. 34 127

[8] Fonck R. J., Ramsey A. T. and Yelle R. W. 1982 Appl. Opt . 212115

[9] Schwob J. L., Wouters A. W., Suckewer S. and Finkenthal M. 1987 Rev. Sci. Insrum.58 1601

[10] Carraro L., Costa S., Puiatti M. E. et al 2000 Plasma Phys.Control. Fusion 42 731

[11] Fournier K. B., Cohen M., May M. and Goldstein W. H. 1988 At. DataNucl. Data Tables 70 231

[12] Kelly R. L. 1987J. Phys. Chem. Ref. Data 16 Suppl.1

[13] National Institute of Standards and Technology (NIST) Atomic Spectra Database: http://aeldata.nist.gov

[14] Summers H P 1994 Atomic Data and Analysis Structure (ADAS) Report JET-IR(94)06 JET Joint Undertaking, Abingdon (England)

[15] Summers H. P. and O'Mullane M. ADAS User Manual, version 2.2 2000 http://patiala.phys.strath.ac.uk/ adas/

[16] Carraro L., Mattioli M., Sattin F. et al 1997 Phys. Scr. 55 565

[17]"Collisions of Carbon and Oxygen Ions with Electrons, H, H2 and He" (edited by Phaneuf R. A., Janev R. K. and Pindzola N. F.) 1987 Oak RidgeNational Laboratory ORNL-6090/V5

[18] Janev R. K., Winter H. P. and Fritsch W. in "Atomic and Molecular Processes in Fusion Edge Plasmas" edited by Janev R. K.), Plenum Press, New York and London (1995) 341

[19] Phaneuf R. A., Janev R. K. and Hunter T. H. 1987 Nucl. Fusion special Suppl 7

[20] Nakai Y., Shirai T., Tabata T. and Ito R. 1989 Phys. Scr. T 28 77

[21] Tawara H., Kato T. and Nakai Y. 1985 At. Data Nucl. Data Tables 32 235

[22] Can C., Gray T. J., Varghese S. L. et al. 1985 Phys. Rev. A 31 72

[23] Meyer F. W., Howald A. M., Havener C. C. and Phaneuf R. A.,1985 Phys. Rev. A 32 3310

[24] Colchin R. J. Brooks N. H., Owen L. W. et al. 2000 Proc. 27th EPS Conf.on Controlled Fusion and Plasma Physics (Budapest) 24B 760

[25] Stratton B. C., Fonck R. J., Ida K. et al. 1986 Rev. Sci. Insrum. 57 2043

[26] Denne B. and Hinnov E. 1984 J. Opt. Soc. Am. B 1 699

[27] Zastrow K. D. and Brzozowski J. H. 1993 Phys. Fluids B 5 4099

[28] Hodge W. L., Stratton B. C. and Moos H. W. Rev. Sci. Insrum. 55 16

[29] Klose J. Z. and Wiese W. L. (1989) J. Quant. Spectrosc. Radiat. Transfer 42 377

[30] Isler R. C. and Langley R. A. 1985 Appl. Opt . 24 254

[31] Carolan P. G., Duval B. P., Field A. R. et al. 1987Phys. Rev. A35, 3454

[32] Carraro L., Puiatti M.E., Scarin P. and Valisa M. 1985 Rev. Sci. Insrum. 66 613

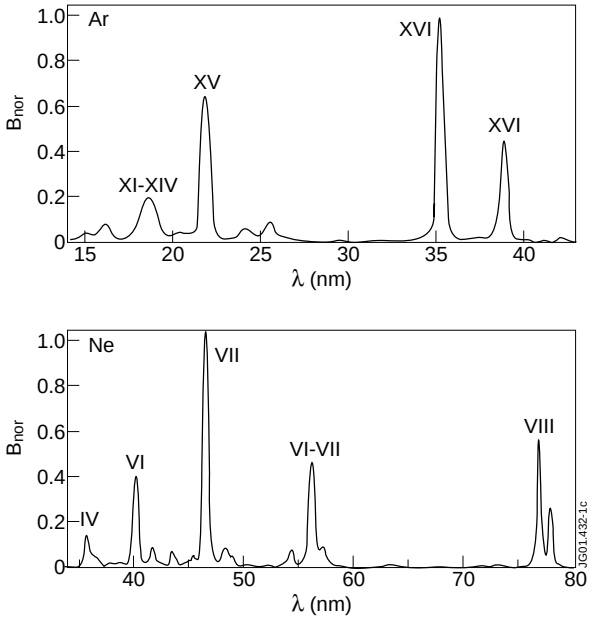

Fig.1: Experimental spectra (with brightness B_{nor} normalized to the strongest line) observed on JET by the SPRED spectrometer along an horizontal line of sight in an argon-seeded discharge (top) and in a neon-seeded discharge(bottom).

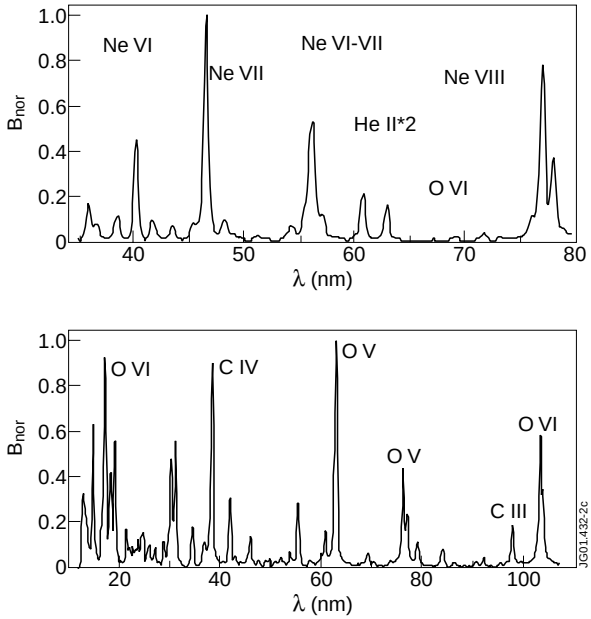

Fig.2: Experimental spectra (with brightness B_{nor} normalized to the strongest line) observed on RFX by the SPRED spectrometer along an horizontal line of sight in a neon-seeded discharge (top) and with intrinsic impurities only (bottom).

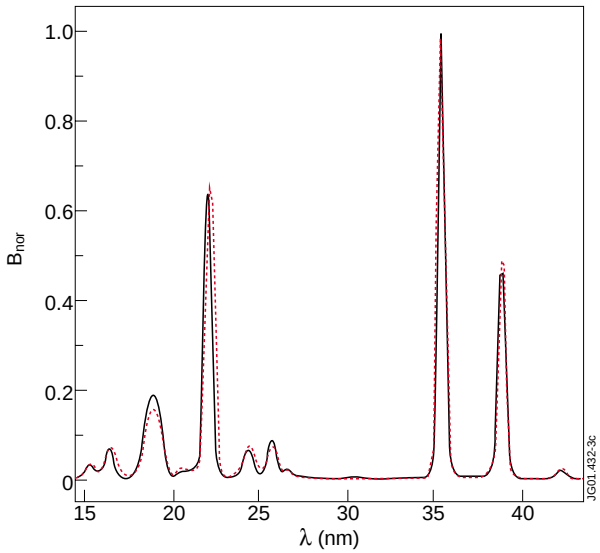

Fig.3: Comparison of the simulated JET argon spectrum with the experimental one in the range 15-45nm (broken and full curves, respectively). The instrumental function assumed to simulate the experimental brightness B_{nor} (normalized to the strongest line) is a Gaussian curve with FWHM=0.45nm.

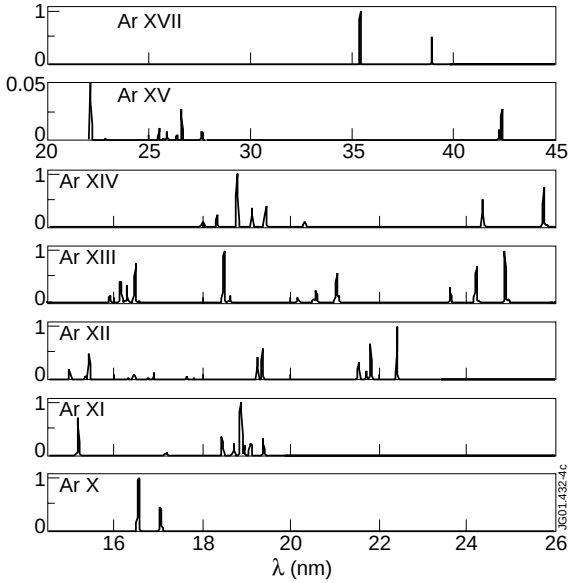

Fig.4: The simulated spectrum of Fig.3 is decomposed in 7 normalized simulated spectra emitted by a single ionization degree from Ar XVI to Ar X. Note that Ar XV scale has been expanded to show the weak lines.

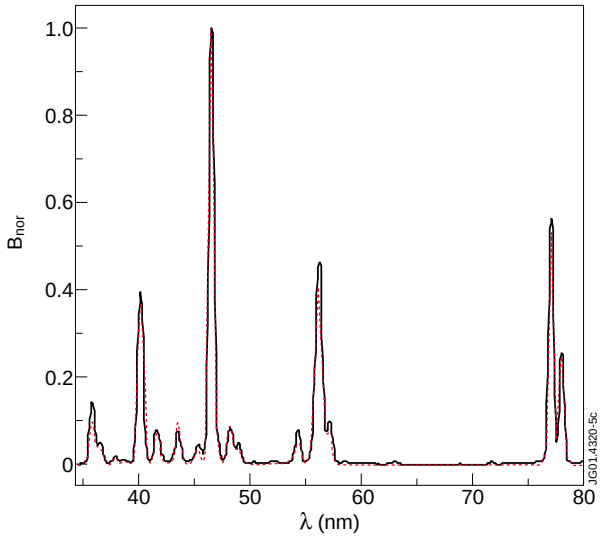

Fig.5: Comparison of the simulated JET neon spectrum with the experimental one in the range 35-80nm (broken and full curves, respectively). The instrumental function assumed for the simulated emissivities is a Gaussian curve with FWHM=0.45nm.

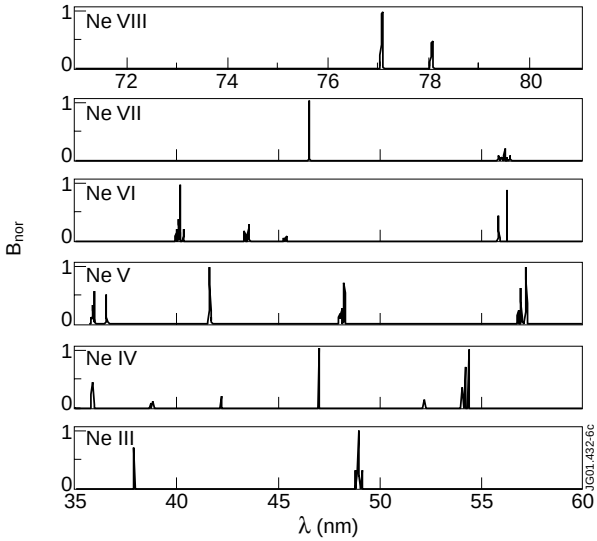

Fig.6: The simulated spectrum of Fig.5 is decomposed in 6 normalized simulated spectra emitted by a single ionization degree from Ne VIII to Ne III.

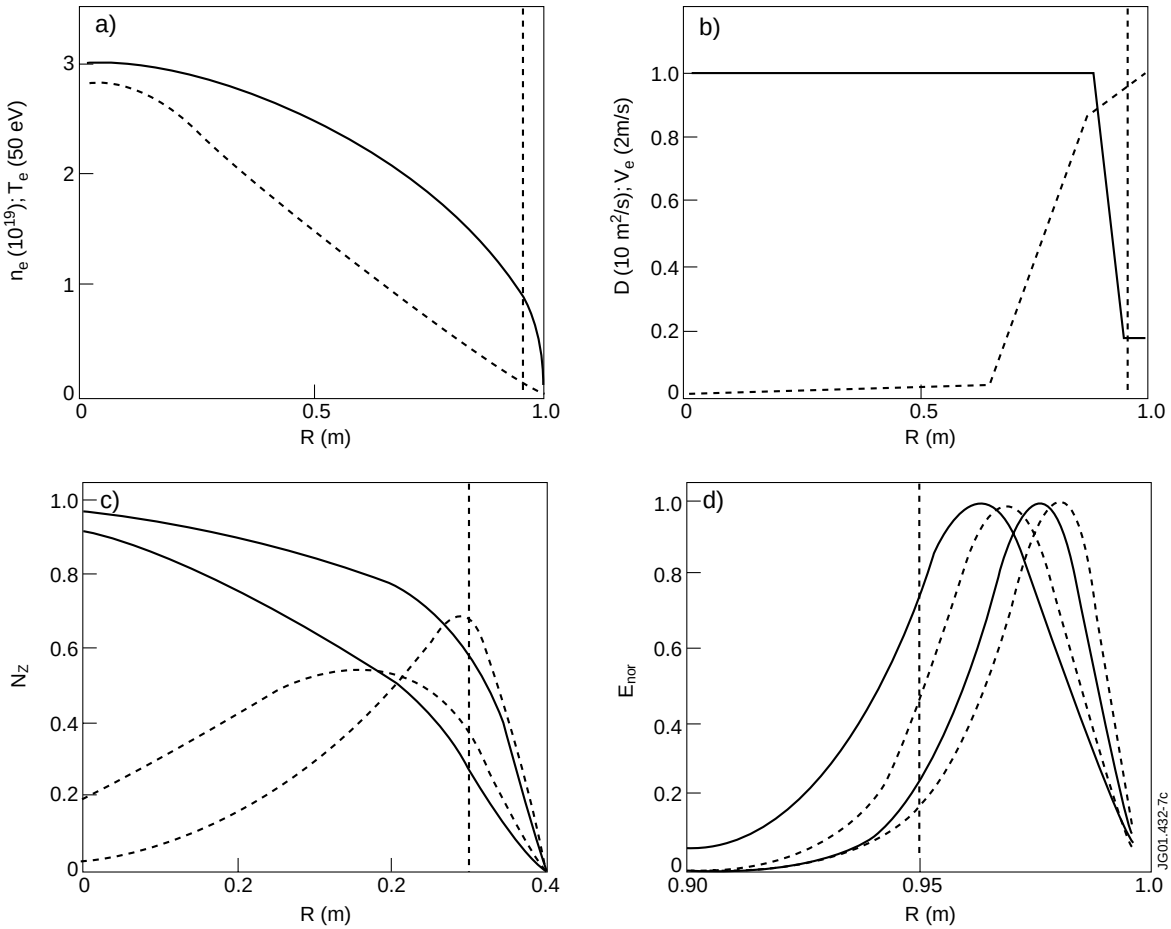

Fig.7: For the simulation of the JET neon-seeded discharge, radial profiles of: a) n_e (full curve) and T_e (broken curve); b) diffusion coefficient D (full curve) and convective velocity V (broken curve); c) neon ion densities (from Ne^{4+} to Ne^{10+}) normalized to the total neon density (full curve): from Ne^{4+} to Ne^{7+} (full curves) multiplied by 10, from Ne^{8+} to Ne^{9+} (broken curves) multiplied by 4) and Ne^{10+} (full curve); d) normalized emissivities of four neon lines from Ne V to Ne VIII (alternatively full and broken curves). The position of the LCMS (broken line) is also indicated.

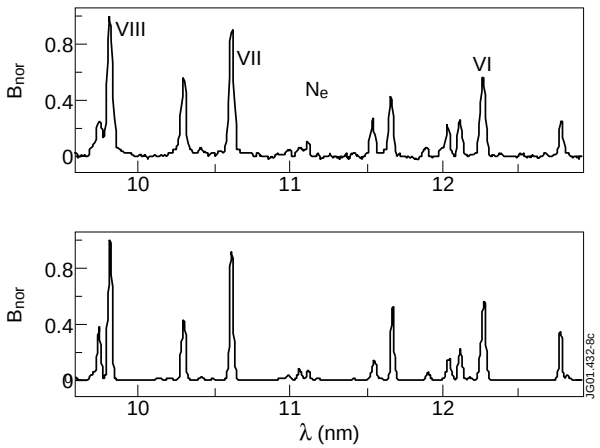

Fig.8: Normalized experimental (top) and simulated (bottom) JET neon spectra in the range 9.6–12.9nm.

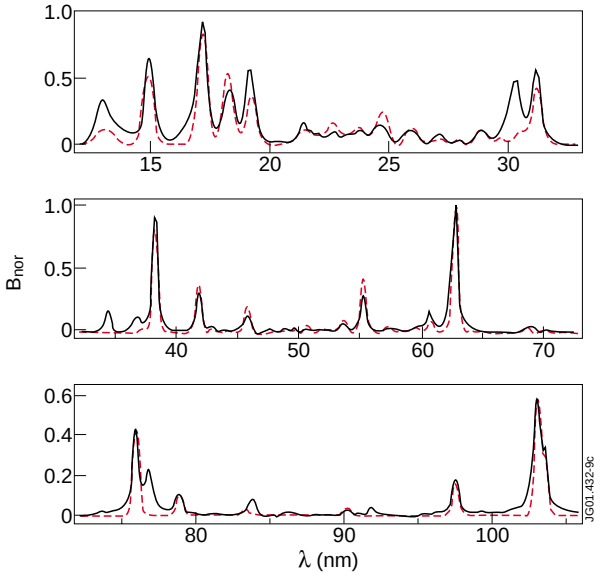

Fig.9: Simulation of the RFX spectrum with only intrinsic impurities between 12 and 105nm, obtained by adjusting the spectrometer sensitivity. The brightness B_{nor} are normalized to the strongest O V line at 63nm. The broken and full curves are, respectively, for the simulation and the experiment.

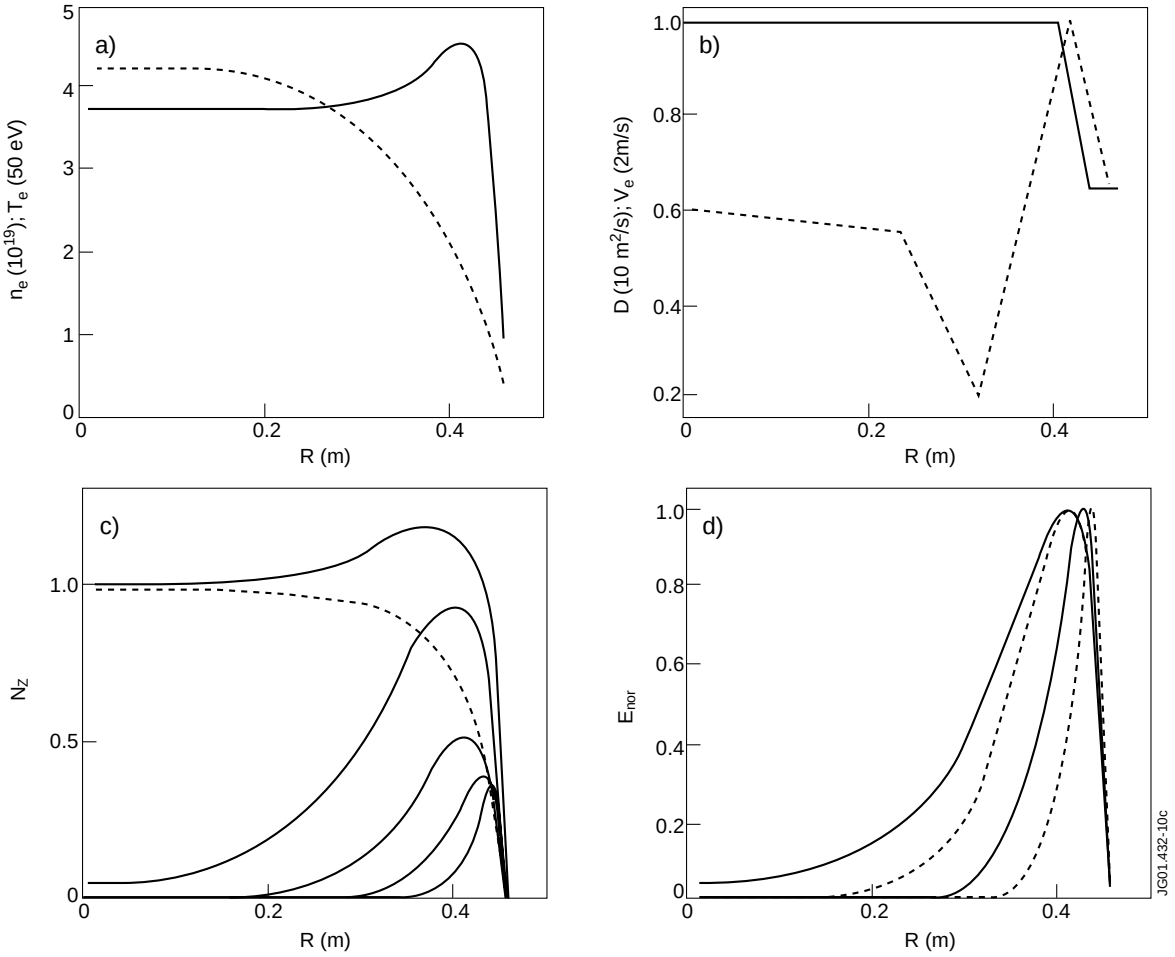

Fig.10: For the simulation of a RFX non-seeded discharge, radial profiles of: a) n_e (full curve) and T_e (broken curve); b) diffusion coefficient D (full curve) and convective velocity (broken curve); c) neon ion densities (full curves from Ne^{4+} to Ne^{7+} multiplied by 4, broken curve Ne^{8+}) normalized to the total neon density (full cur{ ¡°8d) normak¡zecÿemissivities of four neon lines from Ne V to Ne VIII (alternatively full and broken curves).

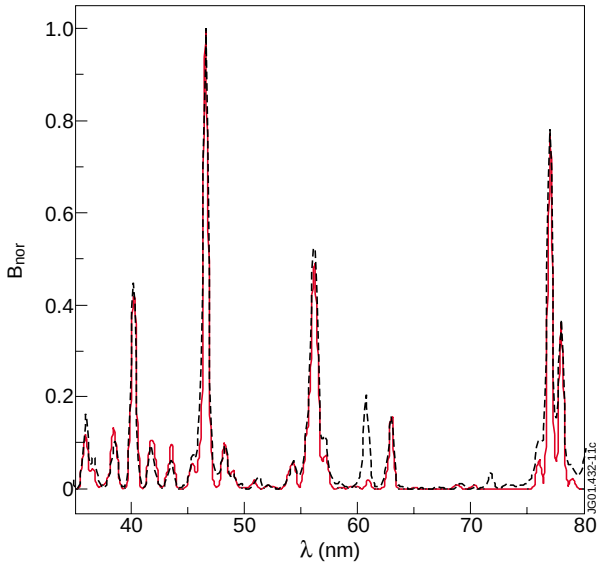

Fig11: Comparison of the simulated and experimental RFX spectra in neon-seeded discharge as obtained by the SPRED spectrometer in the range 35–80nm. The brightnesses B_{nor} are normalized to the strongest Ne VII line at 46.5nm. The broken and full curves are, respectively, for the simulation and the experiment.

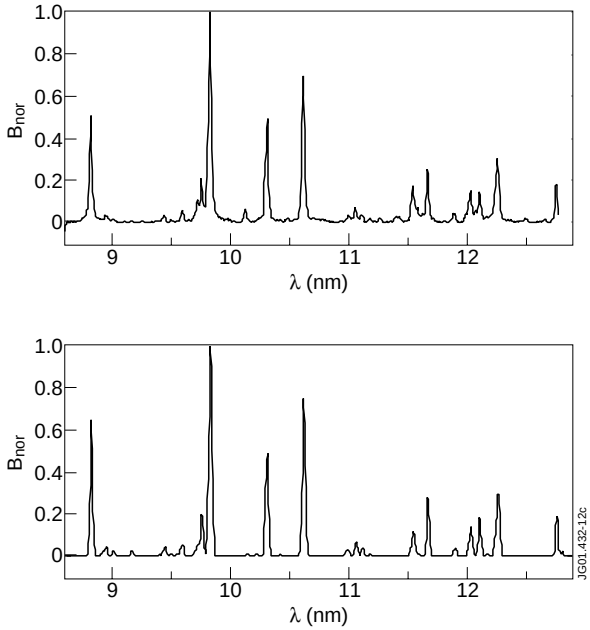

Fig.12: Experimental (top) and simulated (bottom) RFX neon spectra in the range 8.5–13nm.

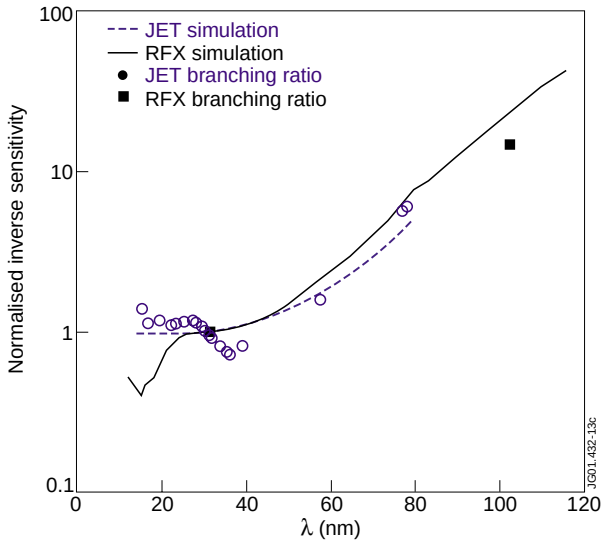

Fig.13: Inverse sensitivity of the SPRED spectrometer installed on JET (broken curve) and on RFX (full curve) as obtained from the simulations, Data obtained from branching ratio for JET (open circles) and for RFX (full squares) are also shown.